Angular-dependent magnetization reversal processes in artificial spin ice

D. M. Burn, M. Chadha, and W. R. Branford
Department of Physics, Imperial College London, London SW7 2BZ, United Kingdom
(Received 30 September 2015; published 17 December 2015)

The angular dependence of the magnetization reversal in interconnected kagome artificial spin ice structures has been studied through experimental MOKE measurements and micromagnetic simulations. This reversal is mediated by the propagation of magnetic domain walls along the interconnecting bars, which either nucleate at the vertex or arrive following an interaction in a neighboring vertex. The physical differences in these processes show a distinct angular dependence allowing the different contributions to be identified. The configuration of the initial magnetization state, either locally or on a full sublattice of the system, controls the reversal characteristics of the array within a certain field window. This shows how the available magnetization reversal routes can be manipulated and the system can be trained.

DOI: 10.1103/PhysRevB.92.214425 PACS number(s): 75.60.Ch, 75.75.Cd, 75.78.Cd

I. INTRODUCTION

Modern lithographic techniques allow for the fabrication of metamaterials where material properties can be engineered through nanoscale structuring giving rise to additional behavior not present in the original material. By patterning arrays interconnected magnetic bars, strong shape anisotropy effects govern the magnetization orientation resulting in an Ising macrospin behavior. Localized magnetic charges can be supported at the interconnections and the ability to manipulate magnetic charges in the form of magnetic domain walls (DWs) provides the basis for novel technological devices including information processing [1] and through the manipulation of bio- or chemically functionalized magnetic nanoparticles [2–6]. Additionally, the patterning of "artificial spin ice" geometries can give rise to a large number of energetically equivalent states, which has been explored in both dipolar coupled systems [7,8] and interconnected networks [9]. Such structures have been suggested for macroscopic studies of fundamental frustrated phenomena and their associated emergent behavior showing strong links to the thermodynamics of the system [10].

The field driven manipulation of pre-existing DWs in connected artificial spin ice systems is governed by the chirality and topological nature of the DW [11,12] and its time-evolution during dynamic propagation [13,14]. These DWs typically originate at the edges of the sample as the reversal in the center of the array is constrained by the magnetization of the surrounding bars [15]. Therefore the magnetization reversal in one bar triggers the reversal in neighboring bars and leads to chains of reversal following Dirac strings in an avalanchelike behavior [15–17]. Furthermore, in isolated bar systems, monopole chirality may provide additional factors that influence the reversal paths in such systems [18].

Varying the angle of the applied field with respect to the geometrical structuring also offers a route to influence the magnetization reversal by biasing particular sublattice directions. Here the angular dependence of the nucleation of a DW from a vertex has revealed an angular shift in the minimum DW nucleation field due to an asymmetric magnetization distribution at the vertex [15,19,20]. Numerical analysis based on this offset model predicts the order of reversal for the different sublattices and the sequences of these reversals [19].

Here, the role of the nucleation process for a DW at the vertices is explored in detail through a series of micromagnetic simulations and experimental measurements on artificial spin ice structures. The reversal fields for both nucleation and DW propagation events vary with angle and our results differentiate between these reversal modes. We also show how the initial magnetization of a structure can affect the angular dependence to the reversal modes in the system.

II. EXPERIMENTAL

Experimental measurements were performed on artificial spin ice structures formed from arrays of interconnected bars arranged in a kagome geometry. The dimensions of the bars were varied including widths of 70 and 150 nm, lengths of 700 nm and 1 μm, and a fixed thickness of 10 nm. These structures were patterned by electron beam lithography in 50 μm $\times$ 100 μm windows followed by the thermal evaporation and lift-off of NiFe onto a Si/SiO_2 substrate.

Focussed magneto-optical Kerr effect (MOKE) microscopy was used to probe the magnetization in the center of these structures in response to applied magnetic fields. This field varied sinusoidally at 1 Hz and was sufficient to saturate the magnetization in the structures. The field was applied along the MOKE poling direction and at an angle θ to the artificial spin ice structuring as illustrated in Fig. 1. The magnetization response was probed over a $\sim$10 μm footprint from a focused laser projected onto the sample. The Kerr signal was averaged over 100 field cycles to enhance the signal to noise ratio of the measurements.

The magnetic field was supplied from a quadrapole magnet capable of applying any vector field in the sample plane. In addition to the 180° field reversals, the magnetization reversal behavior was also investigated from various remanent states after saturation along the three sublattice orientations. This allows control over the initial magnetization of the system and limits the reversal behavior in the remaining bars in the system giving further insight into the magnetization reversal processes within these systems.

Experimental work has been supported by micromagnetic simulations [21] based on zero-temperature numerical modeling, which gives an understanding of the field-driven energetic processes in these structures. Here, typical micromagnetic parameters for permalloy are used: saturation magnetization, $M_S = 860 \times 10^3$ A/m, exchange stiffness, $A = 13 \times 10^{-12}$

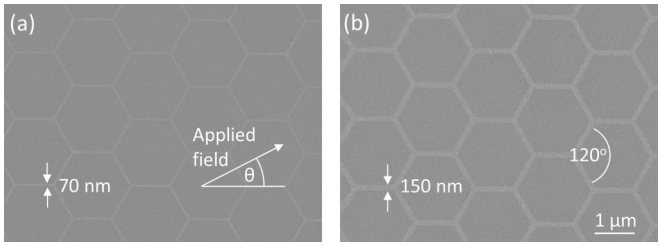

FIG. 1. Image showing kagome artificial spin ice structures with bar dimensions: (a)70 nm × 1 μm and (b) 150 nm × 1 μm. Magnetic fields are applied at an angle θ relative to the structuring.

J/m, and zero magnetocrystalline anisotropy. An artificially high Gilbert damping parameter of $\alpha = 0.5$ allows exploration of the energy landscape of the system and is reasonable for analysis here in the quasistatic regime.

Simulations were performed on a single vertex structure connecting three bars with a 120° separation. The bars were 100 nm wide and 10 nm thick and were represented in the simulations in a 5 × 5 × 10 nm mesh. The simulations were performed in a 1-μm simulation window, sufficient such that artifacts due to the ends of the bars did not significantly affect the magnetization behavior at the vertex. Initially, the magnetization of the structure was prepared in one of six energetically minimized vertex states according to the magnetization orientation in each bar: 2-in 1-out or 1-in 2-out. For each initial state, a field was applied in 10-Oe steps until the magnetization in all three bars had reversed to align with the applied field direction. This reversal was mediated by DW propagation following the injection of the DW from the vertex at the reversal field. Similar with the experimental measurements, the field in the simulations was applied at an angle θ to the vertex structuring allowing the angular dependence of the reversal field to be investigated.

Micromagnetic simulations were also used to investigate the behavior of the structure with an initial magnetization state containing a DW in one of the bars. The chirality of the DW and the orientation of the magnetization in the other two bars strongly affect the behavior that will be discussed in detail later. In some cases, the DW structure unwinds in zero field relaxing to a 2-in 1-out or 1-in 2-out energetically minimized state. In other cases, the DW becomes pinned at the vertex and the same field protocol was used to investigate the depinning behavior of the DW from the vertex structure.

In addition to the study on the kagome and vertex structures, the magnetization reversal in individual bars was also investigated for comparison. MOKE measurements were performed on 10-nm-thick, 250-nm-wide structures and simulations were performed with 10-nm-thick, 100-nm-wide wires. Again, the magnetization reversal was investigated as a function of applied field angle with respect to the wire axis with the initial magnetization in a remanent state following saturation along the wire axis.

III. RESULTS AND DISCUSSION

MOKE measurements on the kagome artificial spin ice system produced a hysteretic magnetization response to an applied field illustrated by the examples in Fig. 2. These loops

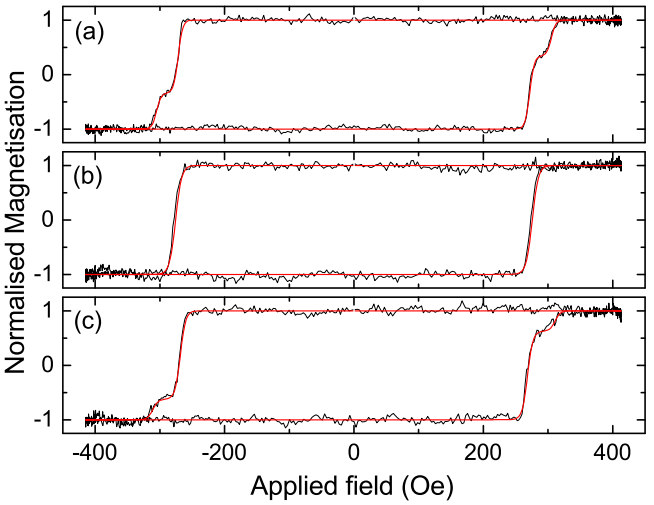

FIG. 2. (Color online) MOKE hysteresis loops for a kagome nanostructured system where the field was applied at (a) 0°, (b) 16°, and (c) 26° to the sample. The line shows a fit to the data.

demonstrate the ferromagnetic behavior of the material that makes up the bars in the sample. Measurements with fields applied at an angle of $\theta = 0°$, 16°, and 26° are shown, and reveal interesting two-step features that occur in the reversal behavior of these samples at certain applied field angles.

The two-step features represent a change in the magnetization which occurs at two distinct fields and represents the behavior of multiple bars within the probed area of the sample. Figure 2 shows the average response measured over 100 field cycles to improve the signal-to-noise ratio. However, this two-step switching can still be identified in single-shot field cycles indicating that multiple reversal processes take place within each field cycle. Our results do not represent a statistical ensemble of reversal events taking place at either a high or low field.

To further investigate these contributions to the magnetization reversal, the steps in Fig. 2 have been fitted with tanh functions [22] parameterized by a reversal field, a magnetization change, and the sharpness of the transition.

Figure 3 shows the angular dependence of the magnetization reversal field for kagome artificial spin ice structures obtained from many hysteresis loop measurements at different field angles. This is shown for two artificial spin ice structures with different bar geometries. The figure reveals a 60°-rotational symmetry, which corresponds to the rotational symmetry of the kagome geometry. This angular dependent behavior is more significant in the greater of the two reversal fields found for the majority of applied field angles. The lower-field reversal event takes place at a field value that stays approximately constant with angle.

The wider bar geometries in Fig. 3(b) result in lower reversal fields than for the thinner bars in Fig. 3(a). This can be attributed to the lower nucleation fields expected for reversal processes in larger structures. Samples with 700-nm-long bars were also characterized and compared with the structures with 1-μm-long bars. The bar length shows a negligible effect on the reversal behavior in comparison to the bar width. This dependence is linked to the relative size of the bars and the

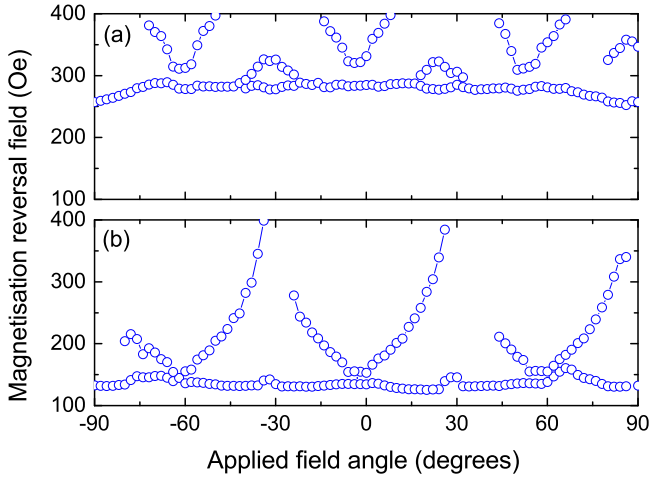

FIG. 3. (Color online) MOKE measurements of the angular dependence of the magnetization reversal fields in kagome artificial spin ice structures with bar geometries (a) 70 nm × 1 μm and (b) 150 nm × 1 μm.

width of a DW. Since the bars are much longer than the width of the DW, the length is not significant in the DW reversal process, which is discussed later.

The kagome artificial spin ice structure can be described as an array of bars arranged in three sublattices where the bars in each sublattice are rotated by 120°. A simplified model for the angular dependence to the reversal field can then be based on three copies of the angular-dependent reversal field for an individual bar. As the angle between the field and the artificial spin ice structure varies, this effectively changes the weighting of the field along the axis of the bars in the three sublattices.

Further insight can be gained by first characterizing the behavior of a single bar as a function of the applied field angle. In this case, only a single jump in magnetization is found in the hysteresis loops and the angular dependence to this switching field is shown in Fig. 4. Both experimental results [Fig. 4(a)]

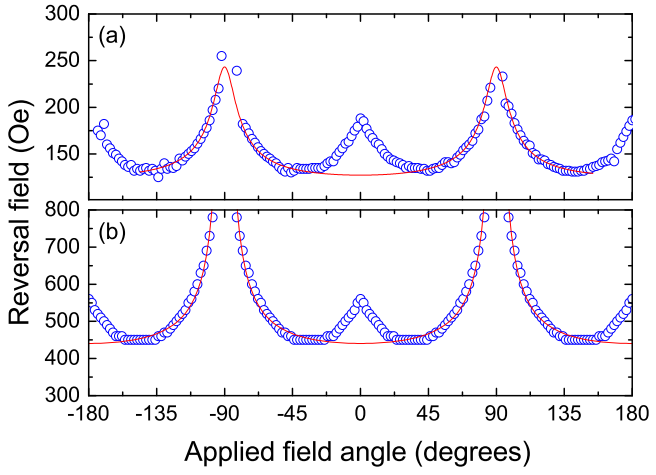

FIG. 4. (Color online) Angular dependence of the magnetization reversal field for a single bar: (a) measured experimentally by MOKE magnetometry and (b) obtained from micromagnetic simulations. The lines show a fit to the models representing curling.

and micromagnetic simulations [Fig. 4(b)] reveal a 180°-rotational symmetry corresponding to the geometry of the bar.

The magnetization reversal in a single bar is typically mediated by the propagation of a magnetic DW along the length of the bar [23,24]. This reversal takes place at a field governed by the nucleation field for the DW where a shift to lower fields in the experimental results can be accounted for by the larger bar dimensions. More significantly, the angular dependence to this field can be modeled by the initial reversal of a small activation region within the wire [25,26], described by the reduced nucleation field for the curling model in an infinitely long cylinder:

$$h_n = \frac{a(1+a)}{\sqrt{a^2 + (1+2a)\cos^2\theta}}. \quad (1)$$

In this expression, the parameter $a = -1.08(2\lambda_{ex}/d)^2$ represents the ratio between the exchange length λ_{ex} and the cross sectional geometry of the wire, $d = \sqrt{t \times w}$ [26].

The model provides a good fit to the angular dependent reversal fields for large angles but does not explain the smaller increase in reversal field when the field is applied along the axis of the bar. Other work on similar nanowire structures also shows this increase in reversal field at small angles as the wire width approaches the exchange length [25,27–29] and may be reminiscent of the Stoner-Wohlfarth coherent reversal behavior taking place [25].

Our understanding of the angular dependent magnetization reversal in one bar provides a basis on which to describe the reversal in the kagome structure with three sublattices of nanobars. By superimposing the behavior of three individual bars with 120° separation, Fig. 5(b) shows the angular dependence of the system that is expected when the effect of the vertices are omitted. The results for the individual bars can be compared to simulations on vertex structures, which connect three bars with a 120° opening. The insert in Fig. 5(a) shows the angular dependent reversal field for the 1-in 2-out state shown. Here, the horizontal and lower branches of the structure are reversed by the field but the magnetization in the upper branch is already aligned with the field so no reversal takes place. The combination of simulations for each initial vertex state is shown in Fig. 5(a). Both Figs. 5(a) and 5(b) clearly show an angular dependent reversal behavior with features repeated every 60° in good agreement with the experimental results in Fig. 3.

The reversal of the horizontal bar, as indicated in the inset in Fig. 5(a), at 0°, takes place after a DW is injected into this bar from the vertex. With a further increase in field, a second DW nucleates at the vertex and propagates along the lower bar. As the angle is increased, the field becomes more favorably aligned with the upper bar leading to a reduction in the reversal field for the horizontal bar. However, the component of the field along the axes of the lower bar decreases resulting in an increase in the field required for reversal of the lower bar.

For angles below −2° in the inset in Fig. 5(a), an extrapolation of the reversal field for the lower bar would give a field below that of the horizontal bar. A reversal of just the lower bar would result in a 3-out monopole defect state with a high magnetostatic energy cost. This state is not predicted by the micromagnetic simulations and instead the

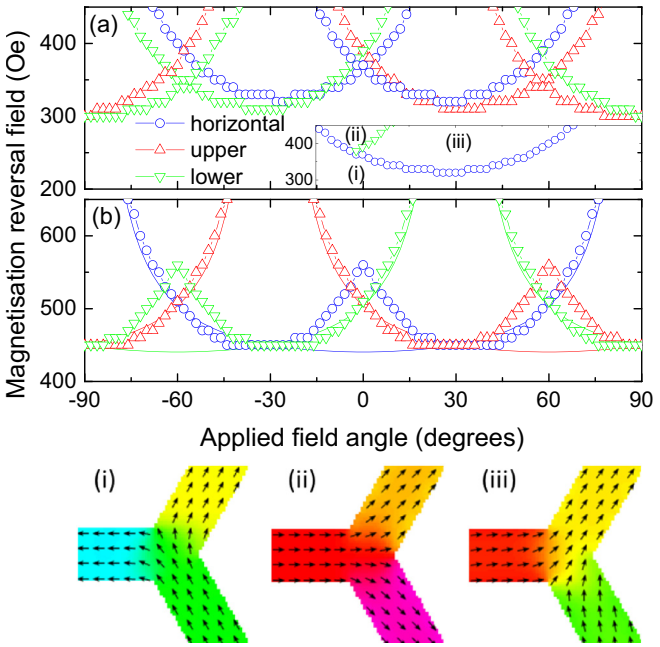

FIG. 5. (Color online) Reversal fields for each bar of a vertex structure as a function of applied field angle. The results are compiled from a series of micromagnetic simulations of (a) a single vertex with different starting configurations and (b) an individual wire plotted three times with a ±60° shift. (i, ii, and iii) indicate the different micromagnetic states shown on the insert of (a).

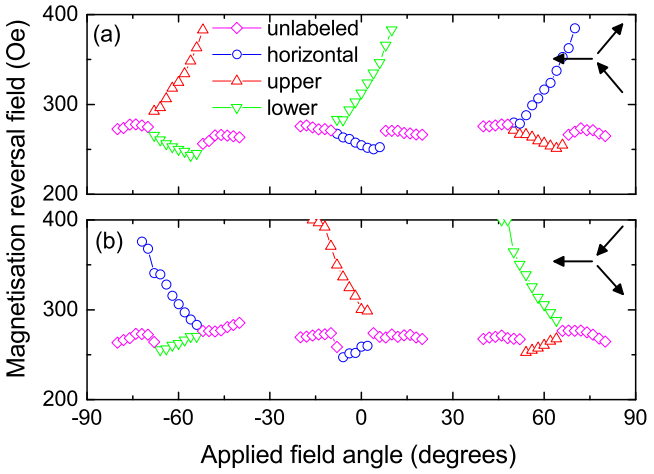

FIG. 6. (Color online) Angular dependence to the reversal field with an initial asymmetric magnetization distribution at each vertex. Where the measured reversal corresponds to the reversal of a single sublattice bar direction this has been labeled. Data at ±30° and ±90° are not recorded due to limitations in preparing the desired initial magnetization state.

system remains in its initial state until the field reaches the reversal field of the horizontal bar. At this point, a DW is injected into the horizontal bar followed by the injection of a DW into the lower bar at the same field.

The curve representing the switching field for the horizontal bar in the inset in Fig. 5(a) is asymmetrical about $\theta = 0°$, which has previously been attributed to the asymmetric magnetization distribution at the vertex [15,19]. Considering the initial 1-in 2-out state with opposite magnetization in the two angled bars, the asymmetry at the vertex reverses. The collective results in Fig. 5(a) show a similar curve with a minimum at $-30°$ revealing symmetric behavior about $\theta = 0$. In this case, for angles close to 0° it is the upper bar that reverses instead of the lower bar.

Comparing the micromagnetic simulations of three bars connected at a vertex [Fig. 5(a)] with three independent bars [Fig. 5(b)] shows many similarities in their behavior but there are some important and subtle differences due to the effect of the vertex. Firstly, the reversal fields are reduced when the vertex is included. This can be attributed to the effective widening of the bar width at the vertex allowing DW nucleation to take place at a lower field. At 0°, the isolated bars show a departure from the curling model with the emergence of a localized peak in the reversal field. When connected at a vertex, this peak appears as two intersecting curves representing the reversal field from two different asymmetric magnetization states at the vertex. Therefore the combination of bars at the vertex gives rise to a degeneracy in the reversal field for the horizontal bar based on the magnetization state of the angled bars.

The micromagnetic simulations indicate that the different curves representing the reversal behavior are related to biasing of the field along the three sublattices in the kagome artificial spin ice structure. This has also been explored through further MOKE measurements by isolating the reversal from particular sublattice bars. Such measurements are performed using more complex applied field protocol involving rotating fields in the plane of the sample [13,19]. Figure 6 shows the angular dependence to the reversal field measured for the 70-nm-wide bars with an initial asymmetrical magnetization distribution at the vertex as illustrated in the figure. Again a 60°-rotation symmetry is observed relating to the rotational symmetry of the structure. However, an asymmetry in the reversal behavior about the bar axis emerges due to the asymmetry of the magnetization state at the vertices. The figure can be understood as repeats of the behavior between $-30°$ and 30°.

In Fig. 6(a), between $-30°$ and 30°, the greater of the two reversal fields increases with angle. This is consistent with the reversal of the lower bar of the vertex structure found from micromagnetic simulations [see insert in Fig. 5(a)]. Since the upper bar is already magnetized in the direction of the field, no reversal events are measured for bars in this sublattice providing the asymmetry in the figure. Figure 6(b) shows the opposite behavior when the initial magnetization is reversed. In this case, the lower bars do not contribute to the reversal and the reversal field for the upper bars increasing with decreasing angle.

The lower reversal field in Fig. 6 also shows features at low angles that were not observed in Fig. 3. This corresponds to a modification in the reversal behavior for the horizontal bar and is also represented by the degeneracy in the reversal field of the horizontal bar in Fig. 5(a) for the different vertex states.

In this work so far, the higher field magnetization reversal events are linked to DW propagation triggered by the nucleation of a DW at the vertex. However, the lower field showing a consistent reversal field and the appearance of peaks in the reversal at ±30° in Fig. 3 is not explained by these simple nucleation processes. To explain these, we consider the role of pre-existing DWs and their mobility through the system.

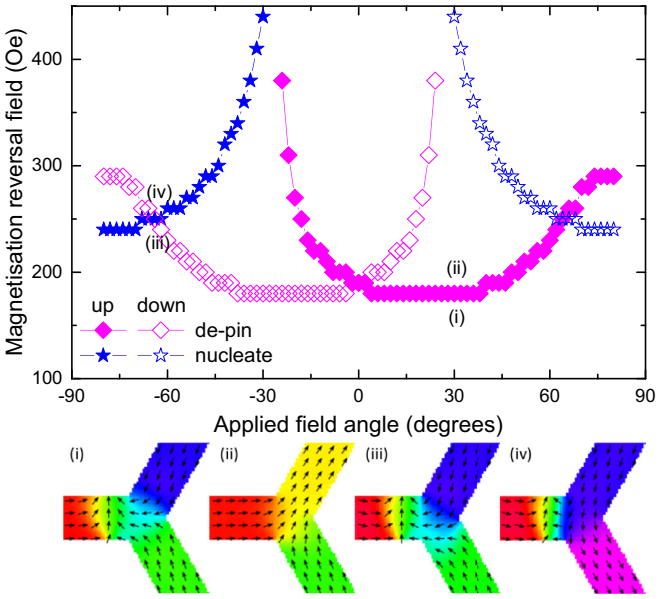

FIG. 7. (Color online) Micromagnetic simulations showing the field required to depin or nucleate a secondary DW from a vertex structure. The micromagnetic structure is shown at the labeled points where an initial up-chirality DW was present in the horizontal bar.

The interaction between the DW and the vertex depends on the spin texture at the vertex and also of the structure and chirality of the DW. Dynamical effects lead to time-dependent variations in these components and are also important to fully describe the system. Here, a simplified modeling approach in the quasistatic regime provides sufficient understanding for qualitative comparison with the experimental results, which also only show the average over both bar directions.

First, considering a vertex with symmetric magnetization in the two angled bars and a transverse DW initially in the horizontal bar. With increasing applied field the DW approaches the vertex, undergoes a micromagnetic structural rearrangement during its interaction, eventually de-pinning at a depinning field, which is discussed in detail elsewhere [13]. The angular dependence to this depinning field is shown in Fig. 7 for both up- and down-chirality DWs where an asymmetry about the wire axis originates from the chirality of the DW.

Topological constraints govern the path of the DW at the vertex resulting in the up-chirality DW taking the upper branch. However, if the field is supplied at a negative angle beyond -30° then the simulations reveal that the original up-chirality DW remains pinned at the vertex and a secondary DW nucleates and propagates along the lower branch. Similarly, a down-chirality DW becomes pinned with a field applied at an angle greater than 30° and a secondary DW nucleates in the upper branch. As the field approaches this $\pm 30^\circ$ change in behavior, the reversal field shows a discontinuity.

Qualitative comparison can be drawn between the micromagnetic simulations with a pre-existing DW in Fig. 7 and with the experimental results in Fig. 3. Since the MOKE results show an average over many vertex reversal events, information about the DW chirality is not present. However, the angle independent lower field reversal measured experimentally is represented by the largely angle independent reversal field for angles -30° to 30°. The repetition of this behavior to match the 60°-rotational symmetry of the system would result in field independent behavior over the entire angular range and may provide an explanation for this feature in the experimental results. Additionally, the peak-shaped increase in reversal field at $\pm 30^\circ$ due to the change in behavior from de-pinning to nucleation of a DW is reminiscent of the peaks observed in Fig. 3 at these angles. Our micromagnetic analysis of a transverse DW shows a better comparison with the 70-nm-wide wires in Fig. 3. The modified behavior observed for the 150-nm-wide wires may represent variations in the DW spin structure, possibly towards vortex DWs, which become stable in wider wires.

For completeness, DW interactions with vertices with asymmetrical magnetization distributions were also investigated. When the chirality of the DW has a magnetization component which aligns with that of the vertex, this leads to the unwinding of the DW into the vertex structure. This results in either a 2-in 1-out or 1-in 2-out structure where a DW can nucleate at the vertex following the behavior described earlier. When the magnetization in the DW opposes the asymmetrical magnetization of the vertex, the DW cannot unwind and instead becomes pinned at the vertex and does not take part in any further magnetization change.

IV. CONCLUSIONS

In conclusion, we have performed an experimental and micromagnetic investigation into the magnetization reversal behavior in interconnected artificial spin ice systems. This reversal is mediated by the propagation of magnetic DWs along the interconnecting bars and reversal events are found to occur at two distinct fields. The greater of these fields displays rotational symmetry corresponding to the structural geometry of the artificial spin ice. Micromagnetic simulations of DW nucleation at a vertex describe these higher field reversal events relating to the variation in field bias along particular sublattice bar directions. Limitations on allowed bar reversals are imposed to avoid monopole defect states at the vertices with high magnetostatic energy cost.

Simulations including initial DW structures within one of the bars give an angular dependent reversal behavior which is reminiscent to some of the features found in the experimental results. These features are not explained by the nucleation of DWs at the vertex. This study of the angular dependence of the magnetization shows physical differences between the DW nucleation and propagation processes allowing the different contributions to be identified within an artificial spin ice structure. The configuration of the initial magnetization state, either locally or on a full sublattice of the system, controls the reversal characteristics of the array within a certain window of field strength and angle. This shows how the magnetization reversal routes available to the system can be manipulated and the system can be trained.

ACKNOWLEDGMENT

The authors acknowledge valuable discussions with L. F. Cohen and financial support from The Leverhulme Trust under RPG 2012-692.

[1] D. A. Allwood, G. Xiong, C. C. Faulkner, D. Atkinson, D. Petit, and R. P. Cowburn, Science **309**, 1688 (2005).
[2] G. Ruan, G. Vieira, T. Henighan, A. Chen, D. Thakur, R. Sooryakumar, and J. O. Winter, Nano Lett. **10**, 2220 (2010).
[3] E. Rapoport, D. Montana, and G. S. D. Beach, Lab Chip **12**, 4433 (2012).
[4] E. Rapoport and G. S. D. Beach, Appl. Phys. Lett. **100**, 082401 (2012).
[5] P. Vavassori, V. Metlushko, B. Ilic, M. Gobbi, M. Donolato, M. Cantoni, and R. Bertacco, Appl. Phys. Lett. **93**, 203502 (2008).
[6] M. Donolato, P. Vavassori, M. Gobbi, M. Deryabina, M. F. Hansen, V. Metlushko, B. Ilic, M. Cantoni, D. Petti, S. Brivio, and R. Bertacco, Adv. Mater. **22**, 2706 (2010).
[7] R. F. Wang, C. Nistor, R. S. Freitas, J. Li, W. McConville, B. J. Cooley, M. S. Lund, N. Samarth, C. Leighton, V. H. Crespi, and P. Schiffer, Nature **439**, 303 (2006).
[8] S. Zhang, I. Gilbert, C. Nisoli, G-W. Chern, M. J. Erickson, L. O'Brien, C. Leighton, P. E. Lammert, V. H. Crespi, and P. Schiffer, Nature (London) **500**, 553 (2013).
[9] W. R. Branford, S. Ladak, D. E. Read, K. Zeissler, and L. F. Cohen, Science **335**, 1597 (2012).
[10] J. Drisko, S. Daunheimer, and J. Cumings, Phys. Rev. B **91**, 224406 (2015).
[11] K. Zeissler, S. K. Walton, S. Ladak, D. E. Read, T. Tyliszczak, L. F. Cohen, and W. R. Branford, Sci. Rep. **3**, 1252 (2013).
[12] A. Pushp, T. Phung, C. Rettner, B. P. Hughes, S-H. Yang, L. Thomas, and S. S. P. Parkin, Nat. Phys. **9**, 505 (2013).
[13] D. M. Burn, M. Chadha, S. K. Walton, and W. R. Branford, Phys. Rev. B **90**, 144414 (2014).
[14] S. K. Walton, K. Zeissler, D. M. Burn, S. Ladak, D. E. Read, T. Tyliszczak, L. F. Cohen, and W. R. Branford, New J. Phys. **17**, 013054 (2015).
[15] P. Mellado, O. Petrova, Y. Shen, and O. Tchernyshyov, Phys. Rev. Lett. **105**, 187206 (2010).
[16] R. V. Hügli, G. Duff, B. O'Conchuir, E. Mengotti, A. F. Rodríguez, F. Nolting, L. J. Heyderman, and H. B. Braun, Phil. Trans. A **370**, 5767 (2012).
[17] E. Mengotti, L. J. Heyderman, A. F. Rodríguez, F. Nolting, R. V. Hügli, and H. B. Braun, Nat. Phys. **7**, 68 (2010).
[18] N. Rougemaille, F. Montaigne, B. Canals, M. Hehn, H. Riahi, D. Lacour, and J. C. Toussaint, New J. Phys. **15**, 035026 (2013).
[19] Y. Shen, O. Petrova, P. Mellado, S. Daunheimer, J. Cumings, and O. Tchernyshyov, New J. Phys. **14**, 035022 (2012).
[20] S. A. Daunheimer, O. Petrova, O. Tchernyshyov, and J. Cumings, Phys. Rev. Lett. **107**, 167201 (2011).
[21] M. J. Donahue and D. G. Porter, The oommf package is available at http://math.nist.gov/oommf.
[22] B. K. Middleton, M. M. Aziz, and J. J. Miles, IEEE Trans. Magn. **36**, 404 (2000).
[23] K. Shigeto, T. Shinjo, and T. Ono, Appl. Phys. Lett. **75**, 2815 (1999).
[24] R. P. Cowburn, D. A. Allwood, G. Xiong, and M. D. Cooke, J. Appl. Phys. **91**, 6949 (2002).
[25] W. Wernsdorfer, B. Doudin, D. Mailly, K. Hasselbach, A. Benoit, J. Meier, J. P. Ansermet, and B. Barbara, Phys. Rev. Lett. **77**, 1873 (1996).
[26] J. I. Martín, J. L. Costa-Krämer, F. Briones, and J. L. Vicent, J. Magn. Magn. Mater. **221**, 215 (2000).
[27] J-E. Wegrowe, D. Kelly, A. Franck, S. E. Gilbert, and J.-Ph. Ansermet, Phys. Rev. Lett. **82**, 3681 (1999).
[28] R. O'Barr and S. Schultz, J. Appl. Phys. **81**, 5458 (1997).
[29] L. O'Brien, D. E. Read, D. Petit, and R. P. Cowburn, J. Phys. Condens. Matter **24**, 024222 (2012).